JOURNAL OF SOLID STATE CHEMISTRY 96, 141–153 (1992)

HTB-Like Six-Membered Rings of Octahedra in Some New Oxides: Structural Aspects and Related Properties

M. TOURNOUX, M. GANNE, AND Y. PIFFARD

Institut des Matériaux de Nantes, Laboratoire de Chimie des Solides, UMR-CNRS n°110, Université de Nantes, 2, rue de la Houssinière, F 44072 Nantes cedex, France

Received July 12, 1991

The HTB-like six-membered ring of octahedra is the common building unit of all compounds presented in this review. In three of them the entire (001) HTB plane is observed, associated to either XO_4, X_2O_7, or X_3O_9 groups (X = P, Si, Ge). This association can result in a 2D network as in $K_3Sb_3P_2O_{14}, xH_2O$, as well as in a condensation of similar layers leading to the 3D framework observed in $Cs_3Sb_3Ge_2O_{13}$. The 3D framework of $Cs_8Nb_{10}O_{23}\square(Si_3O_9)_2$ appears as the first term of an intergrowth between the pyrochlore and benitoite structural types. These compounds are good ion-exchangers or promising precursors for such materials. Another family of compounds containing HTB-like six-membered rings corresponds to the first term of an intergrowth between HTB and perovskite types. Their physical properties are discussed in relation with the nature of the cations located either in the framework octahedra or in the perovskite and HTB sites.

The purpose of this paper dedicated to P. Hagenmuller, one of the pioneers in the field of oxide bronzes (*1*), is to show the close structural relationship between the hexagonal tungsten bronze (HTB) type and some new structures recently determined in our laboratory and then to describe some of the properties of the corresponding compounds.

Several structural types such as pyrochlore (*2*) and WO_3, $\frac{1}{3}H_2O$ (*3*) are closely related to the HTB first reported by A. Magneli (*4*). Both pyrochlore and $WO_3, \frac{1}{3}H_2O$ are built up from (001) HTB planes, that is to say planes of corner-sharing MO_6 octahedra forming six-membered rings. In the latter, the complete structure stems from the association of such layers along the c axis via corner-sharing of octahedra with a shift of $a/2$ between two adjacent layers. By a dehydration process above 250°C, a metastable form of WO_3 having the empty tunnel structure of the HTB has been obtained by Figlarz (*5*). The layers are then stacked up on top of each other. Another relative position corresponding to a ($2\mathbf{a}/3 + \mathbf{b}/3$) shift in terms of HTB appears in the pyrochlore type; in that case the layers are not directly linked but joined by the intermediary of octahedra (*2, 6, 7*). This three dimensional arrangement delimits interconnected tunnels.

It is well known that this geometry favors ion exchange or ionic conductivity and that the more covalent the framework is, the higher the mobility of monovalent cations. Our interest in this field has motivated our search for new compounds having 2D or 3D frameworks resulting from the association

0022-4596/92 $3.00

by corner sharing of MO_6 octahedra and XO_4 tetrahedra (M = Sb, Nb; X = Si, Ge, P, As). We report on three of these structures containing (001) HTB planes of octahedra and either XO_4, X_2O_7, or X_3O_9 groups. The first one, $K_3Sb_3P_2O_{14},xH_2O$ (*8*), has a layered structure and can easily be ion exchanged in acidic medium, thus leading to a phosphatoantimonic acid which is a very good ion exchanger. There is a very close structural relationship between $K_3Sb_3P_2O_{14},xH_2O$ and $Cs_3Sb_3Ge_2O_{13}$ (*9*) which is a good candidate for ion exchange reactions with smaller alkali ions. The same promising behavior is observed for $Cs_8Nb_{10}O_{23}\square(Si_3O_9)_2$ (*10*) which appears as the first member of an intergrowth between the pyrochlore and benitoïte structural types.

In the course of their study of tungsten bronzes M_xWO_3 with M = K, Rb, Cs, Tl and $x < 0.10$, Hussain and Kihlborg have characterized by high resolution electron microscopy the orthorhombic tungsten bronzes (OTB) family resulting from intergrowths between HTB and WO_3 (ReO_3) types that they called intergrowth tungsten bronze (ITB) (*11*). A few years ago the structure of $Ca_2TlTa_5O_{15}$ was determined from a single crystal (*12*). This structure corresponds to the first term of the intergrowth evidenced by Hussain and Kihlborg, although the formulation of this tantalate is similar to that of the "Banana" $Ba_2NaNb_5O_{15}$ exhibiting the tetragonal tungsten bronze (TTB) type. $(Sb_2O)Mo_{10}O_{30}$ has the same framework as that of $Ca_2TlTa_5O_{15}$ but in this case the perovskite sites are empty and the hexagonal tunnel contains Sb_2O links (*13*).

$K_3Sb_3P_2O_{14},xH_2O$

(*a*) *Description of the Structure*

This compound crystallizes in the rhombohedral system, space group $R\bar{3}m$ with a = 7.147(1) Å, c = 30.936(6) Å, Z = 3 (*8*).

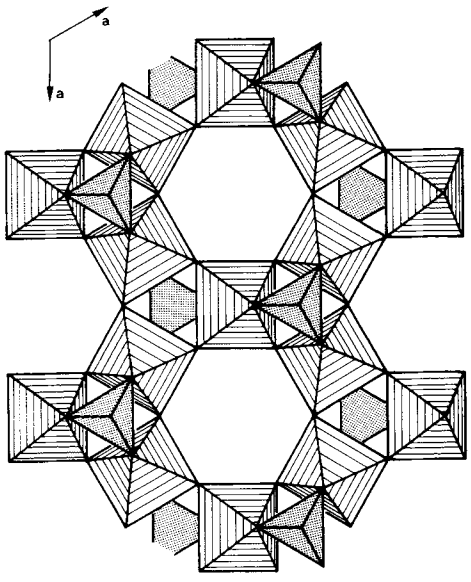

FIG. 1. [001] view of a $(Sb_3P_2O_{14})^{3-}$ layer.

It is a layered material (Figs. 1 and 2). The $(Sb_3P_2O_{14}^{3-})_n$ layers are built up from SbO_6 octahedra and PO_4 tetrahedra sharing vertices. The SbO_6 octahedra are linked together in the same way as the WO_6 octahedra in the (001) HTB plane. The phosphate groups

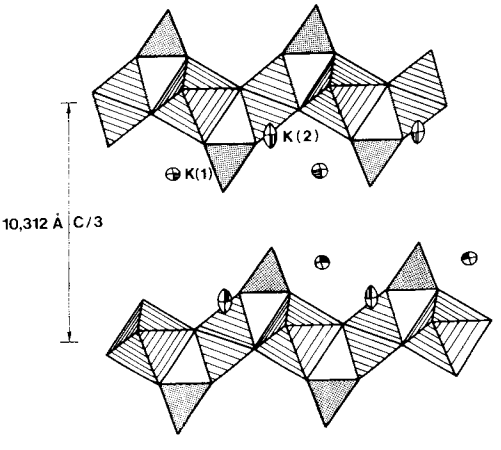

FIG. 2. $K_3Sb_3P_2O_{14},xH_2O$: projection of the structure on (110).

are linked to these layers of octahedra via three of their vertices. The fourth, which is unshared, points into the interlayer space wherein potassium atoms are situated. Similar layers have already been observed in natro- and ammoniojarosites $M^1Fe_3(OH)_6(SO_4)_2$ (*14, 15*) as well as in alunites $M^1Al_3(OH)_6(SO_4)_2$ (*16*).

In the unit cell, there are 9 potassium atoms distributed over 12 possible positions which are therefore occupied at an average of 75%. This compound, prepared by solid state reaction at 1000°C, is hydrated at room temperature (RT). Its water content, inferred from TG experiments and the adsorption isotherm, corresponds to $x = 5$ over almost the whole range of relative humidity (RH) (*17*). The dehydration process which occurs at about 150°C is completely reversible.

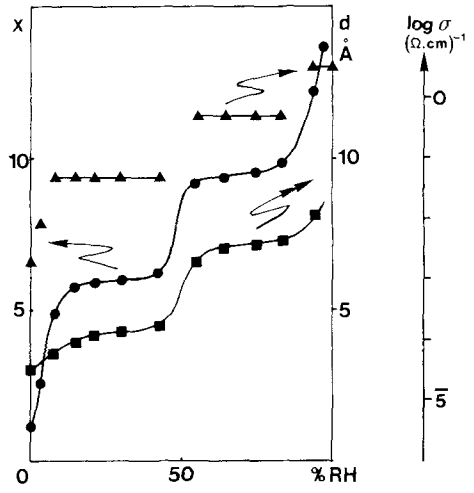

FIG. 3. $H_3Sb_3P_2O_{14},xH_2O$: absorption isotherm of water: evolution of the water content x, of the interlayer distance d and of the conductivity as a function of RH at 20°C.

(*b*) *The Layered Phosphatoantimonic Acid (LPA)* $H_3Sb_3P_2O_{14},xH_2O$

$K_3Sb_3P_2O_{14},xH_2O$ has been ion exchanged in an 8 *N* nitric acid solution at 50°C (*18, 19*). The solution to solid ratio was 100 ml/g of alkali material. After three stages, with renewal of the acidic solution after each 2-hr stage, the extent of exchange is at least 99% and the hydrolysis has proved to be very weak, with less than 1% by weight. Electron and X-ray powder diffraction studies show unambiguously that the covalent layers which have been evidenced in the parent potassium phase are still present in the LPA.

This LPA is hydrated and its water content at RT strongly depends on the partial pressure of water vapor. The RH influence on the composition, interlayer distance, and protonic conductivity has then been studied at 20°C (*20*). The main results of this study have been summarized in Fig. 3. Since the lattice parameters parallel to the layers are very close to those of the parent potassium phase, one can calculate the increase of volume per formula unit of the interlayer space, simply by considering the evolution of the interlayer distance. It is then possible to estimate if the corresponding increase of the water content can be associated, entirely or partly, to crystallization water. For this LPA the protonic conductivity is closely related to the water content (Fig. 3). Each plateau corresponds to a fixed x value and to a particular interlayer distance. Therefore this evolution shows a true "bulk-type" conductivity in agreement with the fact that, from volume considerations, the water content can be associated with crystallization water over almost the whole range of RH.

(*c*) *Acidic and Ion Exchange Properties of* $H_3Sb_3P_2O_{14},xH_2O$

The ion exchange behavior of $H_3Sb_3P_2O_{14},xH_2O$ is illustrated by the titrations with alkali hydroxide solutions (*19*) (Fig. 4) and also by ion exchange isotherms such as those represented in Figs. 5 and 6. The ordinate of these plots, $\bar{X}_M$, is the equivalent fraction of the M^+ ion in the exchanger and the abscissa, X_M, is the equivalent fraction

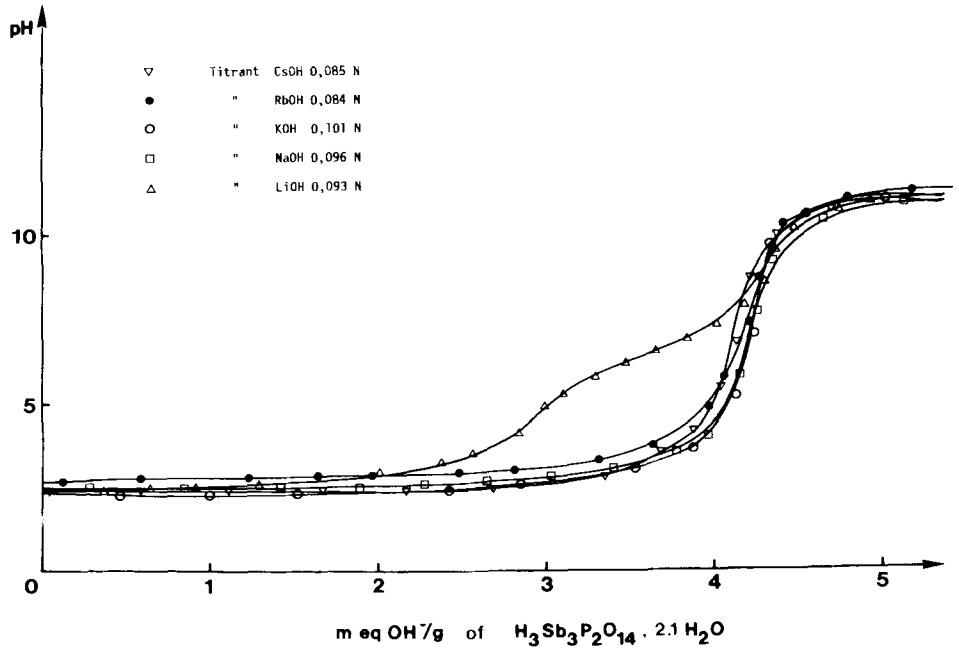

FIG. 4. Potentiometric titration curves for alkali cations on $H_3Sb_3P_2O_{14},xH_2O$.

of the M^+ ion in the solution. Both curves show that the selectivity coefficients of the Cs^+/H^+ and Ag^+/H^+ systems with this LPA are very high.

It has been shown from vibrational studies (*21–23*) that the interaction between acidic protons, as well as all protonic species, and covalent layers is relatively weak. Strongly self-associated HPO_4^{2-} groups similar to those observed in $Zr(HPO_4)_2,nH_2O$ (*24*) do not exist in this LPA in which acidic protons belong to H_3O^+ oxonium groups; this means that it is a stronger acid than α-ZrP like acids which require a preinterca-

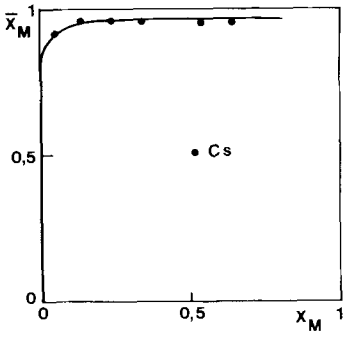

FIG. 5. Cs^+/H^+ ion exchange isotherm on $H_3Sb_3P_2O_{14},xH_2O$.

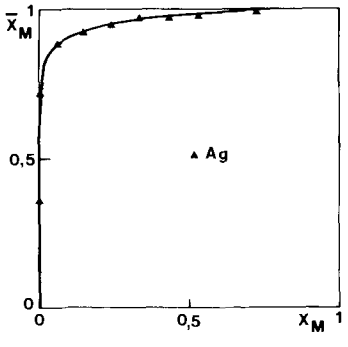

FIG. 6. Ag^+/H^+ ion exchange isotherm on $H_3Sb_3P_2O_{14},xH_2O$.

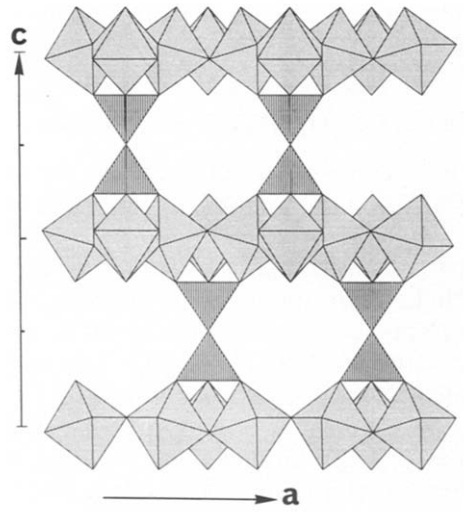

FIG. 7. Projection of the $[Sb_3O_6(Ge_2O_7)]^{3-}$ framework on the (*a*, *c*) plane.

lation of amines to give colloïdal suspensions.

$Cs_3Sb_3Ge_2O_{13}$: Its Relationship with $K_3Sb_3P_2O_{14},xH_2O$

$Cs_3Sb_3Ge_2O_{13}$ crystallizes in the hexagonal system, space group $P6_3/mmc$ with a = 7.31(1) Å, c = 16.73(1) Å, Z = 2 (*9*). Its three-dimensional framework (Fig. 7), built up from SbO_6 octahedra and GeO_4 tetrahedra, can be described as resulting from a condensation of $M_3O_6(XO_4)_2$ covalent layers (M = octahedral cation, X = tetrahedral cation) similar to those which occur in $K_3Sb_3P_2O_{14},xH_2O$. This condensation takes place via the outwardly pointing vertex, as yet unshared, of each XO_4 group. They join to give X_2O_7 groups. In that manner the $(Sb_3Ge_2O_{13})^{3-}$ framework can be considered as HTB-like planes of SbO_6 octahedra linked together by Ge_2O_7 groups so that the hexagonal windows delimited by the six-membered rings are aligned along the c axis. According to this description $Cs_3Sb_3O_6Ge_2O_7$ would be a more relevant chemical formula for this compound. Cs atoms are situated within the large interconnected cavities delimited by this framework. High ion mobility is expected to take place in this phase when ions are exchanged with smaller alkali ions; investigations in this domain are in progress.

$Cs_8Nb_{10}O_{23}\square(Si_3O_9)_2$

This compound crystallizes in the hexagonal system, space group $P6_3/mmc$ with a = 7.342(1) Å, c = 22.166(2) Å, Z = 1 (*10*). The structure consists of a three-dimensional arrangement of NbO_6 octahedra and three-membered Si_3O_9 single rings linked together by corners. It can be described in terms of stacking of planes of polyhedra along the c axis (Fig. 8):

—HTB-like planes of $Nb(1)O_6$ octahedra at $z = 0$ and $\frac{1}{2}$

—planes of separated $Nb(2)O_6$ octahedra at $z = \pm\frac{1}{8}$ and $\pm\frac{3}{8}$

—planes of separated Si_3O_9 rings at $z = \pm\frac{1}{4}$.

As each oxygen atom is connected to two cations (either Nb, Nb; Nb, Si; or Si, Si) the sequence along the c axis can be written $[(Nb(1)_3O_9)\ (Nb(2)O_3)\ (Si_3O_6)\ (Nb(2)O_3)]_{2n}$. It must be mentioned, however, that this type of writing does not account for the relative positions of the two halves of the unit cell. With the same restriction as for relative positions of successive "blocks" (formula written between square brackets), the pyrochlore framework can be described as a $[(M_3O_9)(MO_3)]_{3n}$ sequence (M = octahedral cation) along the [111] axis (*2*), and the benitoite framework by $[(Si_3O_6)(TiO_3)]_{2n}$ along the c axis (*25*). For the title compound, the covalent framework can then be formally considered as an alternance of one pyrochlore- and one benitoite-type "block" (Fig. 8). This description suggests that it is the first member of a family of intergrowths. Preparations of various members have been

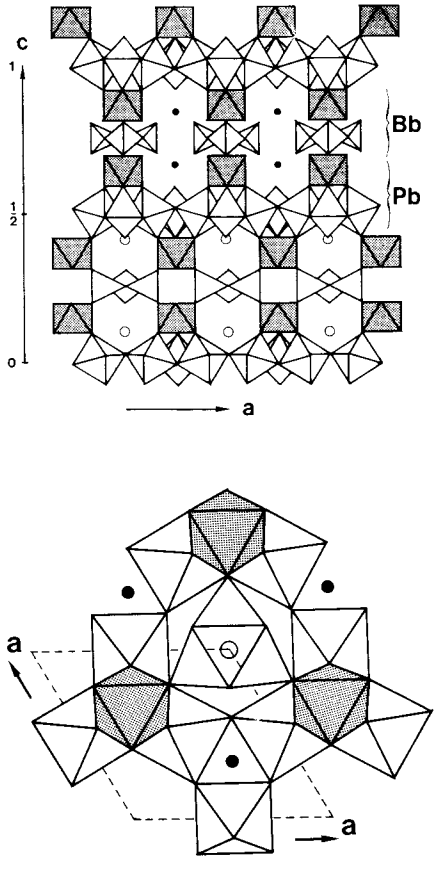

FIG. 8. (a) Fragment of the $Cs_8Nb_{10}O_{23}(Si_3O_9)_2$ structure parallel to the (*a*, *c*) plane, showing the sequence of Pyrochlore blocks (Pb) and Benitoite blocks (Bb). (b) [001] projection of fragment of the structure. $Nb(2)O_6$ octahedra are shaded.

undertaken and they are presently being studied with high-resolution electron microscopy and X-ray diffraction.

In the pyrochlore structure the basic framework per unit cell is $M_{16}X_{48}$ and the volume of the unit cell is about 1100 Å^3, whereas in the title compound the framework is $Nb_{10}Si_6O_{41}\square$, i.e., $M_{16}X_{41}\square$, with a volume of 1035 Å^3. Consequently, with about $\frac{1}{8}$ fewer anions, the structure of $Cs_8Nb_{10}O_{23}\square(Si_3O_9)_2$ can be considered as more open than that of pyrochlore. The ion exchange properties of this compound are presently being investigated.

The $Ca_2TlTa_5O_{15}$ OTB Type Structure

The compounds of general formula $M_2^{II}M^{I}M_5^{V}O_{15}$ crystallize either with the well known tetragonal tungsten bronze (TTB) type first described by A. Magneli (*26*) or with the new structural type that was called orthorhombic tungsten bronze (OTB) when the structure of $Ca_2TlTa_5O_{15}$ was determined a few years ago (*12*).

The structure was refined in the orthorhombic space group *Pmm*2. A projection of the structure along [001] is shown in Fig. 9. As it can be seen, the oxygenated framework is built up from corner-sharing octahedra and is reminiscent of the $(2)_1$ first intergrowth term, of orthorhombic symmetry, reported for the M_xWO_3 bronzes (*11*). For this reason and also because other compounds such as $(Sb_2O)(Mo_5O_{15})_2$ (*13, 27*) or $(Bi_2O)(Mo_5O_{15})_2$ (*28, 29*) which have an analogous oxygenated framework exhibit physical properties of oxide bronzes, this new structural type was called OTB. Octahedra are arranged in such a manner that they de-

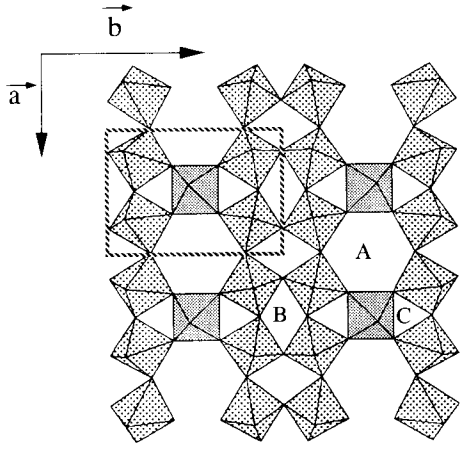

FIG. 9. [001] view of the $(Ta_5O_{15})^{5-}$ framework in $Ca_2TlTa_5O_{15}$, showing the *A*, *B*, and *C* cavities.

limit three types of cavities noted *A*, *B*, and *C* (Fig. 9) whose sections in the (001) plane are respectively hexagon-like, diamond-shaped, and triangular. The larger one (*A*) can accommodate the biggest univalent cations such as Tl^+, Rb^+, or Cs^+ in 18-fold coordination while sites B fit well for divalent cations or trivalent rare-earth cations in dodecahedral coordination (*30*).

Formally the OTB skeleton can originate from the HTB network by one (010) plane out of two with low octahedra density first being eliminated and then the slices so formed, containing six-membered rings of octahedra, being stacked up. This reconstructive process eliminates one *A* and two *C* cavities in HTB and creates two dodecahedral *B* sites in OTB. It results in an intergrowth phase between HTB and perovskite-like sequences. Both OTB and TTB structures are closely related. In particular, the same M_5O_{15} units are found but they adopt a staggered disposition in TTB to form *A'*, *B'*, and *C'* cavities with pentagonal, square and triangular sections respectively. However, crystallographic formulations are different for both structures; they are written $B_2AC_2M_5O_{15}$ and $B'A'_2C'_2M_5O_{15}$, respectively, for OTB and TTB.

For given a $M^{II}_2M^{I}M^{V}_5O_{15}$ formulation one can ask what are the relevant parameters which govern either OTB or TTB.

Relative Stability of Both OTB and TTB Types

The relative stability depends primarily on steric factors. A few years ago, thanks to numerous substitutions, it was established, using an homogeneous scale of crystal radii in eight-fold coordination (so as to compare with TTB), that a simultaneous presence of a large univalent cation in *A* site ($r_{(VIII)} > 1.58$ Å) and a relatively small one in *B* site (1.08 Å $< r_{(VIII)} < 1.19$ Å) favors the OTB type (*30*). On the other hand, the largest divalent cations being in *A'* sites rather determine the TTB type. Of course other factors such as polarization effects also have to be taken into account. These effects are important too in order to explain piezoelectric properties evidenced in some OTB compounds. These properties were discussed in terms of hardness or softness, as defined by Pearson (*31*), of the cations present in *A* and *B* sites. It was shown that the piezoelectric effect in OTB is favored by the presence both of a soft cation in *A* and of hard cations in *B* sites. $Ca_2TlTa_5O_{15}$ and $Ca_2CsTa_5O_{15}$ are piezoelectric but not $Ca_2RbTa_5O_{15}$. Partial substitution in *A* site by smaller cations such as K^+ induces and/or strengthens piezoelectricity because of the off-centering of smaller cations. For instance, $Ca_2Rb_{1-x}K_xTa_5O_{15}$ becomes piezoelectric for $x > 0.15$.

Thermodynamic factors (pressure and temperature) of course influence the stability of either OTB or TTB. For example, $Ca_2TlTa_5O_{15}$ was transformed to TTB at 1273 K under 60 kb. This transformation induces a relative decrease of cell volume $\Delta V/V$ of about 5%. Therefore OTB compactness is lower than the TTB one. Under atmospheric pressure, by raising temperature up to 1900 K, the tetragonal phase $RbGdNaTa_5O_{15}$ was transformed into orthorhombic with a relative increase of cell volume by 2%. Hence it can be thought that the entropy of OTB is higher than that of TTB.

Crystal Field in OTB and TTB Dodecahedral Sites

In order to improve comparison between both types, crystal field was tested in *B* and *B'* sites in order to explain the magnetic behavior of some neodymium and europium phases (*32*). From the splitting values of the Nd^{3+} $^4F_{3/2}$ level on one hand and the Eu^{3+} $^7F_1$ level on the other hand, which almost exclusively depend on crystal field second rank components (B^2_q), it was shown that these latter were higher in OTB (>1000 cm^{-1}) than in TTB (~500 cm^{-1}). B^2_q is re-

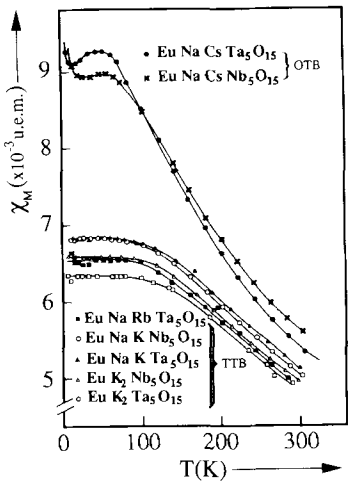

FIG. 10. Thermal evolution of molar magnetic susceptibility in some Eu^{2+} OTB and TTB compounds.

lated to the orthorhombic distortion and acts only in OTB but B_o^2 is present in both symmetries, tetragonal and orthorhombic. In addition the Nd^{3+} $^4I_{9/2}$ ground state splitting value which depends on several B_q^k components is more important in OTB (>800 cm^{-1}) than in TTB (~650 cm^{-1}). This fact indicates higher values for some crystal field components acting at the lanthanide site in OTB.

Comparatively Eu^{3+} is a more suitable local probe than Nd^{3+} for testing crystal field. Indeed looking at magnetic susceptibility curves obtained with powder samples of OTB and TTB europium tantalum compounds in Fig. 10, it can be seen clearly that both types are sharply divided. The characteristic plateau observed at low temperature depends on χ_o constant terms in the Van Vleck formula (*33*) whose values result from a perturbation, in first order approximation, of the ^7F_o ground state by excited states via crystal field operator and particularly the B_q^2 components. According to the plateau values it can be deduced that B_q^2 are higher in OTB.

A further investigation by ^{151}Eu nucleus Mössbauer spectroscopy confirmed that the B_o^2 crystal field component was higher in $EuNaCsNb_5O_{15}$ (OTB) than in $EuK_2Nb_5O_{15}$ or $EuNaKNb_5O_{15}$ of tetragonal symmetry (*32*).

$EuNaCsNb_5O_{15}$: The First Member of a New Class of Ferroelectrics

Given the numerous points of comparison outlined above between OTB and TTB it was natural to search for ferroelectricity in OTB compounds. The first attempts to evidence hysteresis loops at room temperature failed because, as emphasized below, the lattice stiffness is more important in OTB than in TTB. However, the $Ca_2TlTa_5O_{15}$ space group being a polar one, substitutions were performed in order to increase the acentric character of this phase. As it is well established for tetragonal and perovskite-like ferroelectrics, substitution of niobium for tantalum increases Curie temperature. Hence $EuNaCsNb_5O_{15}$ (*28*) was synthetized. Under a 10 $kV.cm^{-1}$ electric field, the hysteresis loop, obtained on sintered samples, appears only at about 500 K, then is saturated at 530 K and disappears near 565 K, the Curie temperature. This behavior is characteristic of a hard ferroelectric. On the other hand it can be observed that ε'_r damping increases with field frequency (Fig. 11). This fact is characteristic of a diffuse transition due to simultaneous presence of two cationic species (Eu^{3+}, Na^+) in dodecahedral *B* sites. Structural determination from a single crystal of $EuNaCsNb_5O_{15}$ in polar space group $Pmc2_1$ reveals that spontaneous polarization is closely related to a sequence of short (1.792 Å) and long (2.137 Å) Nb(1)–O(10) bonds along the *c* axis. The $Nb(1)O_6$ octahedron is located at the center of the M_5O_{15} unit (Fig. 9) (*34*). P_s at 293 K and T_c can be estimated using the empirical formula of Abrahams *et al.* (*35*) to be 45 $\mu C \cdot cm^{-2}$ and 600 ± 30 K respectively (experimental value for T_c: 565 ± 10 K). The

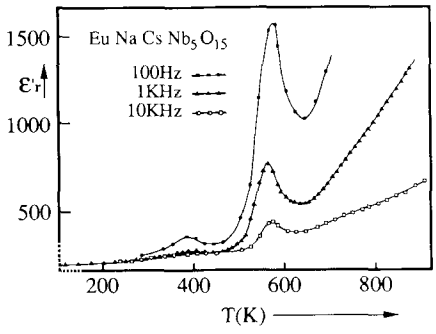

FIG. 11. Frequency and temperature dependence of the dielectric permitivity in $EuNaCsNb_5O_{15}$.

P_s value can be compared with that of "Banana" $Ba_2NaNb_5O_{15}$ ($P_s = 40\ \mu C \cdot cm^{-2}$ at 293 K). The displacive transition is probably of the second order and purely ferroelectric. In TTB ferroelectrics the polar axis lies usually in the (*a*, *b*) plane whereas in this OTB, *c* is the polar axis. Hence this situation renders more difficult the microscopic distortions inducing P_s spontaneous changes and even more since the crystal field strongly stabilizes the perovskite planes. This is why coercive field values are so high below 500 K. Because of its lattice stiffness EuNaCs Nb_5O_{15} exhibits quasi-pyroelectric behavior.

The search for ferroelectricity has not been much developed and other ferroelectric compounds of this large new family could probably be prepared.

The $(Sb_2O)(Mo_5O_{15})_2$ Orthorhombic Type

(*a*) *Structural Features*

The crystal structure of this orthorhombic bronze was determined in the polar space group *Pma*2 (*27*). Projection of the structure along [001] shows clearly (Fig. 12) that the oxygenated network is very similar to that of $Ca_2TlTa_5O_{15}$ and can be formally described as a $(2)_1$ intergrowth term. However, some differences between both types must be outlined. Octahedra inside which Mo atoms are off-centered are very distorted and delimit hexagonal tunnels containing $-Sb_2O-$ units where the Sb^{III} lone pair is stereochemically active. Dodecahedral sites remain empty because the $-Sb_2O-$ link acts as a tetravalent pseudocation. Sb^{III} is linked to two oxygen atoms of the framework and to another one in the tunnel thus adopting the SbO_3E (E lone pair) configuration. Detailed examination of the structure indicates that Sb^{III}–O bonding competes with π Mo–O bonding inside octahedra for $2p\ \pi$ oxygen orbitals of the framework. It results that π bonding becomes localized on some particular bonds causing an off-centering of Mo atoms inside their oxygen polyhedron. Then cooperative ferroelectric distortions along each chain of octahedra are evidenced along the polar axis. Inside the cell, net electric polarization vanishes because polar chains order antiferroelectrically thus yielding a supercell (which contains four Mo_5O_{15} units). From these structural features can be anticipated the presence of narrow bands and flat levels in this antimony compound.

(*b*) *Band Model of the* $(Sb_2O)(Mo_5O_{15})_2$ *Semiconductor*

Transport properties measurements of this mixed valence compound (40% Mo^V,

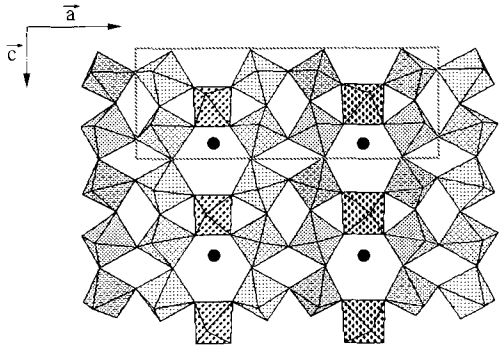

FIG. 12. [001] view of the $(Sb_2O(Mo_5O_{15})_2$ structure showing off-centered Sb atoms in the *A*-channels.

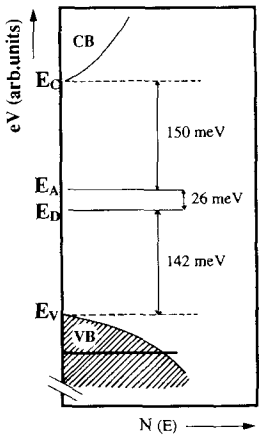

FIG. 13. Band model for $(Sb_2O)(Mo_5O_{15})_2$.

60% Mo^{VI}) were performed on sintered bars of polycrystalline samples (90% compactness) between 150 and 500 K. Experimental results including electrical conductivity σ, thermoelectric power S, and Hall coefficient R_H were interpreted by means of a p-semiconductor model with two inverted acceptor and donor deep levels which pin the Fermi level near the mid-gap (*36*). Conduction mechanisms are governed by acoustical-phonon scattering of the carriers. In this bronze the gap value is small (~320 meV) and because of the high positive value of S, hopping conduction was neglected. The band model for antimony molybdenum bronze is depicted in Fig. 13. To account for spin (Mo^V) concentration determined from an E.P.R. experiment, it was necessary to involve flat levels situated below valence band edge far enough not to interfere in conduction mechanisms.

Recent band calculations with tight-binding approximation back up this model and bring more precise information about valence band (VB) and conducting band (CB) nature (*37*). VB is made of four bands mainly built up from "d_{xz}" orbitals of octahedra in perovskite-like sequence whereas CB levels imply Mo(6) orbitals (less distorted octahedron of hexagonal sequence). The calculated indirect gap is about 220 meV. In Fig. 14 very narrow bands appear along c^* and numerous flat levels along a^* and b^*. According to these calculations $(Sb_2O)(Mo_5O_{15})_2$ is a quasi-one-dimensional semiconductor.

Semiconducting Properties of Bismuth Orthorhombic Bronze $(Bi_2O)(Mo_5O_{15})_2$

In order to study the influence of M_2^{III}–O units in hexagonal tunnels the bismuth bronze $(Bi_2O)(Mo_5O_{15})_2$ was synthesized. Its cell is a $2a, 2b, 2c$ superstructure of $(Sb_2O)(Mo_5O_{15})_2$ reference cell. To account for transport properties measured on sintered bars of polycrystalline samples, the band model already used for antimony analogue was retained (*38*). Within a 357 meV gap, two inverted deep energy levels separated by 52 meV pin the Fermi level near the mid-gap. Figures 15 and 16 represent thermal carriers ratios and Fermi energy evolutions for both antimony and bismuth semiconductors. Comparatively the carriers ratio p/n is lower in bismuth than in antimony analogues while hole mobility at 300 K is higher (19.7 $cm^2 \cdot V^{-1}s^{-1}$ against 5.4 $cm^2 \cdot V^{-1}s^{-1}$). Here too, spin concentration inferred from E.P.R. measurements ex-

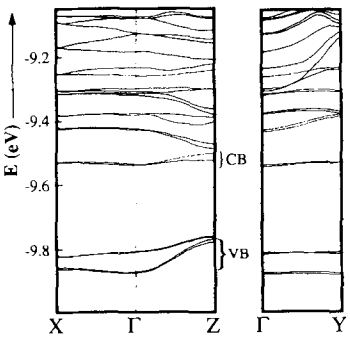

FIG. 14. Calculated band structure for $(Sb_2O)(Mo_5O_{15})_2$.

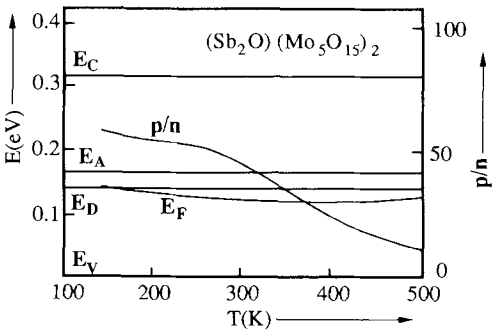

FIG. 15. p/n and E_F evolution in $(Sb_2O)(Mo_5O_{15})_2$.

ceeds by about two orders of magnitude the concentration needed at the N_D donor level to account for semiconductor behavior. Therefore flat levels located below VB band edge where d^1 spins are trapped are postulated. In this compound Bi–O interactions are more ionic than Sb–O interactions; and octahedra are probably more regular; in that case the valence band is larger and the hole mobility higher.

Band Model Extension Applied to Tungsten Phases: $(M_2^{III}O)(W_5O_{15})_2$

Substitution of tungsten for molybdenum and/or bismuth for antimony in OTB bronzes gives rise to numerous phases whose electric behavior depends on compo-

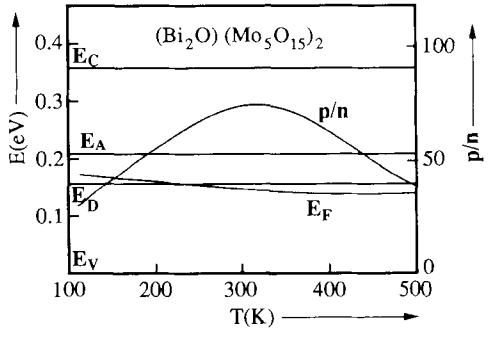

FIG. 16. p/n and E_F evolution in $(Bi_2O)(Mo_5O_{15})_2$.

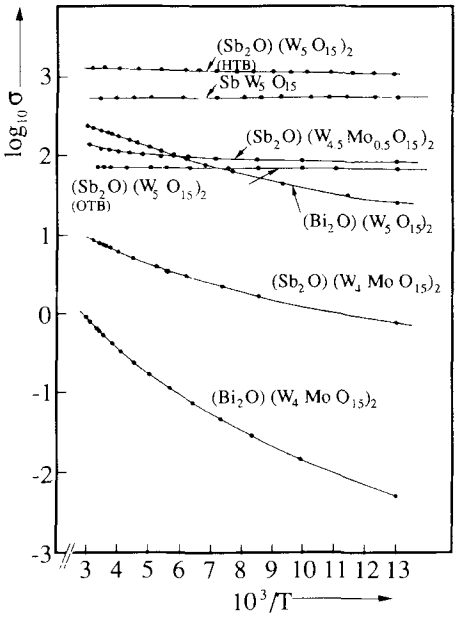

FIG. 17. Evolution of the conductivity with temperature in some OTB phases. One example of HTB compound is given for comparison.

sition and consequently on the structural intergrowth disorder which affects some of these phases. In turn, this disorder depends on temperature, time and heating rate. Our observations corroborate those made about the Sb_xWO_3 system (*39*) in which a first heating treatment, with subsequent annealing, does not modify the structural intergrowth disorder appreciably, whatever heating time. Various phases were synthesized (*28*). It is interesting to outline that $(Sb_2O)(W_5O_{15})_2$ adopts both OTB and HTB structural types depending on temperature. Below 773 K, the HTB type is prepared. An increase of the temperature up to 873 K induces the HTB–OTB transition which evolves slowly and irreversibly. Conductivity measurements were performed on sintered bars of polycrystalline samples (compactness 90%). Variations of the conductivity with temperature for various phases are presented in Fig. 17. Antimony

tungsten compounds, namely $(Sb_2O)(W_5O_{15})_2$ OTB and HTB, are metals whereas $(Sb_2O)(W_4MoO_{15})_2$ and $(Bi_2O)(W_4MoO_{15})_2$ look like semiconductors as it is the case, to a lesser extent, for $(Bi_2O)(W_5O_{15})_2$. As expected for tungsten compounds, conductivity is higher than in molybdenum OTB, 5*d* orbitals having a higher radial extension. Experimental results (S and σ) obtained with $(Bi_2O)(W_5O_{15})_2$ were interpreted by means of a single band model (*40*). The conduction mechanisms are governed by hopping in states near the Fermi energy. It is shown that variable-range hopping occurs at low temperatures while next-neighbor hopping takes place at higher temperatures. This band may originate from overlapping of corresponding VB and CB in molybdenum compounds. This band is less than half filled and the electronic states are highly delocalized leading to "metallic" behavior as observed in $(Sb_2O)(W_5O_{15})_2$.

Conclusion

As illustrated by the examples given in this review, HTB-like six-membered rings of octahedra and even complete slices of the HTB framework perpendicular to either [001] or [100] appear as building units for the structure of many oxides which exhibit a widespread range of properties.

HTB slices perpendicular to [001] associated with XO_4, X_2O_7, or X_3O_9 groups lead to good ion exchangers or promising precursors for such materials.

HTB slices perpendicular to [100] and perovskite slices form the $(2)_1$ intergrowths. This framework is an alternative to the TTB structural type for compounds of general formula $M_2^{II}M^{I}M_5^{V}O_{15}$. According to the nature of the cations located either in their framework octahedra or in the perovskite or HTB sites, various physical properties such as ferroelectricity and semiconductor or metal behavior are observed. A band model recently supported by band calculation makes it possible to interpret the transport properties.

References

1. P. HAGENMULLER, "Comprehensive Inorganic Chemistry," Vol. 4, p. 541, Pergamon, Elmsford, NY (1973).
2. F. JONA, G. SHIRANE, AND R. PEPINSKY, *Phys. Rev.* **98,** 903 (1955).
3. B. GÉRARD, G. NOWOGROCKI, AND M. FIGLARZ, *J. Solid State Chem.* **38,** 312 (1981).
4. A. MAGNELI, *Acta Chem. Scand.* **7,** 315 (1953).
5. M. FIGLARZ, *Prog. Solid State Chem.* **19,** 1 (1989).
6. B. DARRIET, M. RAT, J. GALY, AND P. HAGENMULLER, *Mater. Res. Bull.* **6,** 1305 (1971).
7. M. A. SUBRAMARIAN, G. ARAVAMUDAN, AND G. V. SUBBA RAO, *Prog. Solid State Chem.* **15,** 55 (1983).
8. Y. PIFFARD, A. LAGHGAR, AND M. TOURNOUX, *J. Solid State Chem.* **58,** 253 (1985).
9. C. PAGNOUX, A. VERBAERE, Y. PIFFARD, AND M. TOURNOUX, *Eur. J. Solid State Inorg. Chem.*, in press.
10. M-P. CROSNIER, C. PAGNOUX, D. GUYOMARD, A. VERBAERE, Y. PIFFARD, AND M. TOURNOUX, *Eur. J. Solid State Inorg. Chem.*, in press.
11. A. HUSSAIN AND L. KIHLBORG, *Acta Crystallogr. Sect. A: Found Crystallogr.* **32,** 551 (1976).
12. M. GANNE, M. DION, A. VERBAERE, AND M. TOURNOUX, *J. Solid State Chem.* **29,** 9 (1979).
13. M. PARMENTIER, C. GLEITZER, AND R. J. D. TILLEY, *J. Solid State Chem.* **31,** 305 (1980).
14. C. B. BROPHY, E. S. SCOTT, AND R. A. SNELLGROVE, *Am. Mineral.* **47,** 112 (1962).
15. H. SABINA AND R. TRAIL, *Pap.—Geol. Surv. Can.* **60,** 4 (1960).
16. R. WANG, W. F. BRADLEY, AND H. STEINFINK, *Acta Crystallogr.* **18,** 249 (1965).
17. A. LACHGAR, S. DENIARD-COURANT, AND Y. PIFFARD, *J. Solid State Chem.* **73,** 572 (1988).
18. M. TOURNOUX AND Y. PIFFARD, French Patent 85-01839 (1985).
19. Y. PIFFARD, A. VERBAERE, A. LACHGAR, S. DENIARD-COURANT, AND M. TOURNOUX, *Rev. Chim. Miner.* **23,** 766 (1986).
20. S. DENIARD-COURANT, Y. PIFFARD, P. BARBOUX, AND J. LIVAGE, *Solid State Ionics* **27,** 189 (1988).
21. E. HUSSON, A. LACHGAR, AND Y. PIFFARD, *J. Solid State Chem.* **74,** 138 (1988).
22. E. HUSSON, F. GENET, A. LACHGAR, AND Y. PIFFARD, *J. Solid State Chem.* **75,** 305 (1988).
23. E. HUSSON, M. DURAND-LE FLOCH, C. DOREMIEUX-MORIN, S. DENIARD-COURANT, AND Y. PIFFARD, *Solid State Ionics* **35,** 133 (1989).

24. P. COLOMBAN AND A. NOVAK, *J. Mol. Struct.* **177,** 277 (1988).
25. VON K. FISCHER, *Z. Kristall.* **129,** 222 (1969).
26. A. MAGNELI, *Ark. Kemi* **1,** 213 (1949).
27. M. PARMENTIER, C. GLEITZER, A. COURTOIS, AND J. PROTAS, *Acta Crystallogr. Sect. B* **25,** 1963 (1979).
28. M. DION, Ph.D. Thesis, Nantes (1984).
29. A. CONAN, A. BONNET, M. GANNE, AND M. DION, *J. Phys. Chem. Solids* **46**(6), 721 (1985).
30. M. DION, M. GANNE, AND M. TOURNOUX, *Mater. Res. Bull.* **15,** 121 (1980).
31. R. G. PEARSON, *Chem. Br.* **3,** 103 (1967).
32. M. GANNE, M. DION, G. A. FATSEAS, AND C. LEVY-CLEMENT, *Ann. Chim. Fr.* **11,** 95 (1986).
33. J. H. VAN VLECK, "The Theory of Electric and Magnetic Susceptibility," Oxford University Press, London/New York (1932).
34. M. DION, M. GANNE, M. TOURNOUX, AND J. RAVEZ, *J. Solid State Chem.* **53,** 422 (1984).
35. S. C. ABRAHAMS, S. K. KURTZ, AND P. B. JAMIESON, *Phys. Rev.* **172,** 551 (1968).
36. A. BONNET, A. CONAN, H. QUEINNEC, M. GANNE, AND M. DION, *Phys. Rev. B. Condens. Matter* **30**(2), 688 (1984).
37. E. CANADELL *et al.*, private communication.
38. A. CONAN, A. BONNET, M. GANNE, AND M. DION, *J. Phys. Chem. Solids* **46**(6), 721 (1985).
39. T. EKSTRÖM, M. PARMENTIER, AND R. J. TILLEY, *J. Solid State Chem.* **34,** 397 (1980).
40. A. BONNET, A. CONAN, M. MORSLI, M. GANNE, AND M. TOURNOUX, *Phys. Status Solidi B* **150,** 225 (1988).